Quantitative probing of the fast particle motion during the solidification of battery electrodes (3)

Cite as: Appl. Phys. Lett. **116**, 081904 (2020); https://doi.org/10.1063/1.5144889 Submitted: 13 January 2020 . Accepted: 12 February 2020 . Published Online: 27 February 2020

Yang Yang, Zhengrui Xu, James D. Steiner, Yijin Liu 🗓, Feng Lin, and Xianghui Xiao 🗓

COLLECTIONS

E

This paper was selected as Featured







ARTICLES YOU MAY BE INTERESTED IN

Temperature-dependent nonmonotonous evolution of excitonic blue luminescence and Stokes shift in chlorine-based organometallic halide perovskite film

Applied Physics Letters 116, 072104 (2020); https://doi.org/10.1063/1.5135389

Engineering skyrmions and emergent monopoles in topological spin crystals Applied Physics Letters 116, 090501 (2020); https://doi.org/10.1063/1.5139488

A maximum extreme-value distribution model for switching conductance of oxide-RRAM in memory applications

Applied Physics Letters 116, 082901 (2020); https://doi.org/10.1063/1.5141951





Quantitative probing of the fast particle motion during the solidification of battery electrodes (5)

Cite as: Appl. Phys. Lett. **116**, 081904 (2020); doi: 10.1063/1.5144889 Submitted: 13 January 2020 · Accepted: 12 February 2020 · Published Online: 27 February 2020







Yang Yang, ¹ Zhengrui Xu, ² James D. Steiner, ² Yijin Liu, ³ h Feng Lin, ² and Xianghui Xiao ^{1,a)} h

AFFILIATIONS

- ¹National Synchrotron Light Source II, Brookhaven National Laboratory, Upton, New York 11973, USA
- ²Department of Chemistry, Virginia Tech, Blacksburg, Virginia 24061, USA
- Stanford Synchrotron Radiation Lightsource, SLAC National Accelerator Laboratory, Menlo Park, California 94025, USA

ABSTRACT

Synchrotron x-ray tomography represents one of the most powerful imaging techniques that can visualize the three-dimensional microstructural complexity with a high spatial resolution. To date, however, the temporal resolution of this technique has been handicapped by the intrinsic limitations in the data acquisition speed and the lack of a suitable data processing method. The present study aims to fundamentally resolve this challenge by implementing a data analysis method that is based on differentiating discrete tomography reconstruction from a continuous scan reconstruction. With this methodological development, we capture and quantify the particle motion during the solidification of battery electrodes and reveal the statistics of the dynamically evolving motion in the drying process, which has been challenging to resolve. We discover that the particle motion exhibits a strong dependence on its geometric location within a drying electrode. Our results also imply that the final electrode quality can be controlled by balancing the solvent evaporation rate and the particle mobility in the region close to the drying surface.

Published under license by AIP Publishing. https://doi.org/10.1063/1.5144889

Drying is a common, vital process in manufacturing products of various nature, including but not limited to food, ^{1,2} pharmaceutical products, ^{3,4} materials, ^{5,6} and devices. ⁷ In the drying process, complicated physical and chemical reactions co-exist and intertwine across a wide range of time and length scales. Such a sophisticated interplay collectively governs the drying dynamics, which is fundamental to the formation of the final product. Therefore, complex systems with multifunctional properties and hierarchical structures can be fabricated using well-controlled drying processes. ^{6,7}

During drying of the slurries in the battery electrode formation, phase separation and architectural inhomogeneity take place spontaneously. This can lead to "dead" spots, where the active particles are hardly utilized during battery charging and discharging. As a consequence, many studies have reported the significant charge heterogeneity in battery electrodes. ^{8–11} If different components can be precisely manipulated and assembled into desired three-dimensional (3D) architectures, one may be able to control the distributions of active particles to allow for the ultimate charge homogeneity and the optimal utilization of all the active particles. As the first step toward this goal, one would need to precisely visualize and quantify how active particles move and assemble during the electrode drying process, which has remained one of the major challenges in the battery community.

X-ray microtomography is a nondestructive 3D structure detection technique. In a typical x-ray tomography experiment, a sample is rotated around an axis, and the sample's x-ray shadow images are projected on an x-ray camera and recorded at different rotation angles. The 3D morphological structure of the sample can be reconstructed from the projection images. Fast x-ray microtomography (FXT) based on the synchrotron source has been widely applied to study dynamic phenomena. 12-18 However, it is challenging to apply FXT to study the manufacturing process of battery electrodes. On the one hand, active particles move volatilely and randomly during the drying process, and so a high temporal resolution is required in the measurements to catch these fast and unpredictable motions. Conventionally, this requires a higher probe x-ray flux and faster rotation speed to achieve a higher temporal resolution. On the other hand, the wet slurry sample system is sensitive to the potential heating effects from the high x-ray flux and the disturbance due to the centrifugal force from the fast rotation. There are a few approaches to improve the FXT temporal resolution. 19-22 Although a recent work 21 demonstrated that it is possible to improve the temporal resolution by differentiating discrete tomography scans from a continuous scan that covers a long period, efficient, effective, and precise quantitation of the microstructural evolution remains a daunting challenge.

a) Author to whom correspondence should be addressed: xiao@bnl.gov

In this work, we tackle the frontier challenge of visualizing and quantifying the particle motions during the solidification of battery electrodes using synchrotron-based *operando* FXT measurements and a special data analysis strategy. The proposed data analysis allows for utilizing the conventional FXT data to extract the dynamic information that is beyond the detection limit of the conventional FXT.

A continuous tomography scan scheme, in which a sample is rotated continuously over many revolutions and the sample's projection images are acquired simultaneously, is assumed in this work. Similar to the recent work,²¹ the sample's transient tomographic structures at any given time points can be reconstructed by a tunable data chunking scheme. Differing from the data chunking scheme in the conventional approach, in which a continuous scan dataset is chunked into groups covering every 180° and has no overlap in the angle range, the tunable data chunking scheme chunks the dataset in a way in which the consecutive groups can partially overlap in the angle range. Therefore, we can compare the tomography structures separated by a tunable time gap other than a constant time gap equal to the time T spanning the 180° angle range. This approach differentiates the tomography temporal resolution from T to an arbitrary time gap in a unit of the inverse of the image acquisition rate. Herein, we define it as differential tomography.

In this work, we developed a data analysis method that can provide quantitative structure evolution information even with imperfect tomographic reconstructions with sample motion-induced artifacts. This occurs when the tomography scan rate is slower than the sample structure change rate during the scan period. As discussed in detail in the supplementary material, the centroids of these motion-induced artifacts in a dynamic tomography reconstruction are good approximations to the locations of the corresponding features in the transient structure at the middle time point during the tomography scan. Comparing the imperfect dynamic tomography reconstructions at different time points provides dynamic structure evolution information, e.g., local flow velocity distribution in a drying film at a given time point. Such comparison can be done using the digital volumetric correlation (DVC) technique that is widely used in tomography applications.^{23,24} DVC analysis provides 3D displacement maps. Therefore, dividing the displacement maps by the time gap associated with two structures gives the 3D velocity maps.

We performed a numerical simulation to verify the validity of this approach. In the simulation, there were three types of motions, which are a motion along a straight line at a constant velocity, a motion along a helical trajectory at constant rotational and axial velocities, and a motion along a parabolic trajectory at a constant velocity in one direction and an accelerating motion in the perpendicular direction. Figure 1(a) sketches these three types of motions. Each particle's motion type and motion parameters were randomly initialized. The transient structures at given times were then calculated based on this model. In generating the dynamic tomography dataset, a rotation velocity was assumed. The rotation angle was then correlated with the scan time. The projection images of the simulated tomographic data were generated by projecting the transient structure at the corresponding time along the corresponding angle. To perform the DVC analysis, two dynamic tomography scan datasets and two transient static structure datasets are needed. In the simulation, we assume that each dynamic tomography scan takes 0.5 s. The two dynamic tomography datasets are simulated during the 0-0.5 s time period and 0.45-0.95 s

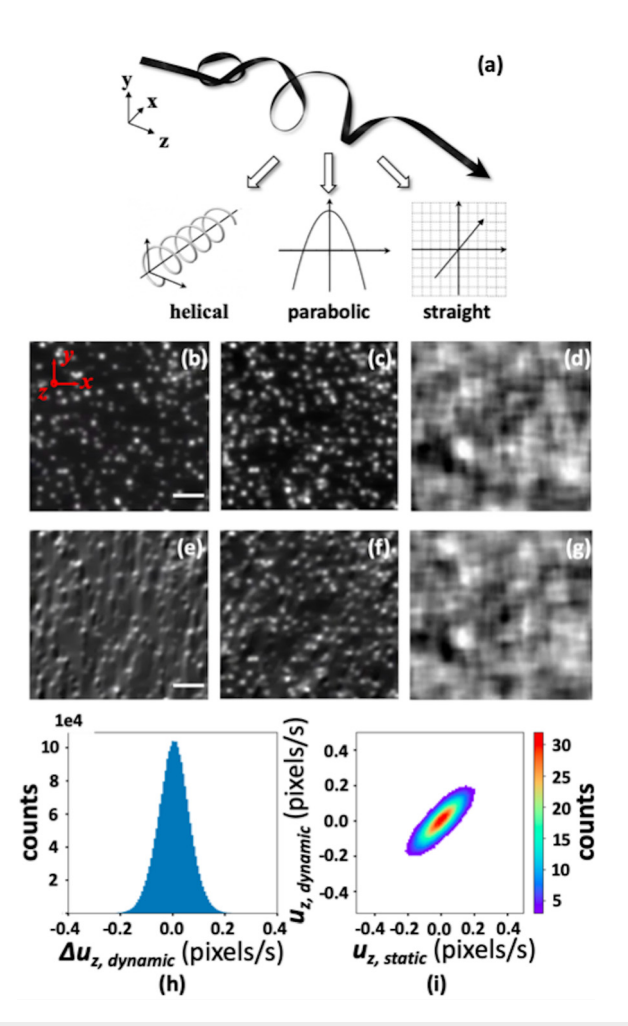


FIG. 1. Simulation results. (a) The sketches of three types of particle motions. (b) and (c) The corresponding 2D slice images in the static structures at times of 0.25 s and 0.70 s, respectively. The global coordinate is defined in (b). (d) z-component displacement $u_{z,static}$ map at the position corresponding to the slices (b) and (c); (e) and (f) the corresponding 2D slice images in the tomography structures reconstructed from tomography scans during periods of 0–0.5 s and 0.45–0.95 s, respectively; (g) $u_{z,dynamic}$ map at the position corresponding to the slices (e) and (f). (h) histogram of Δu_z , and (i) 2D histogram with $u_{z,static}$ and $u_{z,dynamic}$. Scalebars in (b) and (e) are 20 pixels.

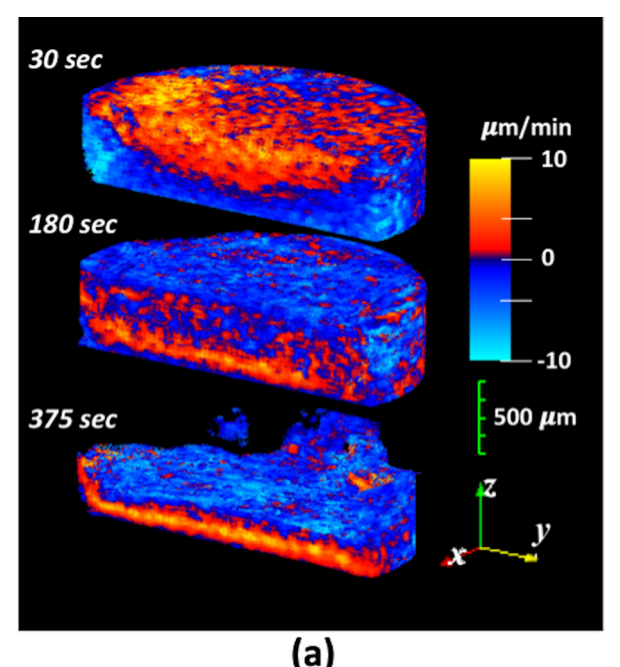
time period. The corresponding static structures are therefore at 0.25 s and 0.70 s. Tomography reconstructions were done using Gridrec algorithm 25,26 in the tomography reconstruction toolkit Tomopy. The DVC analysis with two sets of structures provides the local displacements. Therefore, the local motion velocity distribution in three dimensions is obtained by dividing the displacement map by the time gap between the two datasets. As a definition, the velocity calculated from displacements between the transient structures at two time points is defined as the velocity at the later time point. For instance, the velocity calculated with the structures at 0.25 s and 0.70 s is defined as the velocity at the time point of 0.70 s.

In this work, we used the software Tomowarp 2^{28} for DVC analysis. Figures 1(b) and 1(c) show two slice images from the static

structures at time points of 0.25 s and 0.70 s, respectively. Figure 1(d) shows the corresponding slice image of the z-component displacement from the DVC result with the static structures at time points of 0.25 s and 0.70 s. Accordingly, Figs. 1(e) and 1(f) show the slice images from the dynamic tomographic structures during the scan period of 0–0.5 s and 0.45–0.95 s. Although the motion artifacts are clearly visible in dynamic tomography reconstructions, the displacement map in Fig. 1(g), based on these "imperfect" reconstructed structures, agrees well with the perfect static structures. Figure 1(h) presents the histogram of the difference between Figs. 1(d) and 1(g) and Fig. 1(i) the pixel-topixel correlation between these two displacement maps. The sharp peak around zero in Fig. 1(h) and the narrow band along 45° in Fig. 1(i) suggest a good agreement between the displacement maps calculated with the dynamic tomography structures and the ground truth static structures.

The method was applied to study the drying process associated with lithium-ion battery cathode fabrications. The experiment was done at the beamline 2-BM of the Advanced Photon Source at the Argonne National Laboratory. The slurry was prepared by mixing 450 mg of NMC622 and 25 mg of acetylene carbon black with the polyvinylidene fluoride solution. The average size of NMC622 particles was 10 μ m. A droplet of the slurry was dipped into a bowl-shape container of $3 \times 3 \text{ mm}^2$ cross section and 400 μ m depth that was made of Kapton tape. More details of the sample preparation can be found in the supplementary material. A heating lamp was placed on top of the bowl and turned on before the tomographic scan started. To reduce radiation heating effects onto the sample system, the tomography experiment was done with 40 keV monochromatic x-ray. The sample was continuously rotated for 390 s at a velocity of 6°/s, and 7800 projection images were acquired. The single image exposure time was 50 ms. The slow rotation velocity minimized the potential disturbance due to the centrifugal force to the sample system. Tomography reconstructions were done using Gridrec algorithm in Tomopy. The reconstructed structures are very similar to the simulated data shown in Fig. 1(d), and so the reconstructed cathode particles with motion artifacts served as features in the DVC analysis. The reconstructed 3D images were binned by factor 8 on each dimension to make DVC analysis with Tomowarp2 feasible. The voxel size after binning was 10.4 µm on each dimension. After DVC analysis, the displacement maps were masked by a 3D mask that only covers sample regions at each time point. The mask was obtained using the Trainable Weka Segmentation tool²⁹ available in Fiji software.

The local particle motion velocity maps were calculated at three time points (30 s, 180 s, and 375 s after acquisition started, respectively). Figure 2(a) presents the 3D rendered z-component velocity v_z (along the film depth direction) map at three time points. The results clearly show the heterogeneous local motions in the film. The cross section cuts in these 3D plots clearly show that the v_z map had a domain structure along the film depth direction. Figure 2(b) presents three velocity components averaged in four layers at different film depths at three time points. The first layer is close to the bottom of the container, and the fourth layer is close to the film-air interface at each time point. Another two layers were evenly located between the first and fourth layers. The x- and y-components, v_x and v_y , did not change very much during the entire drying process. After 180 s, the averaged v_x and v_y median values were close to zero because the average particle distance became smaller along with the drying process. Consequently,



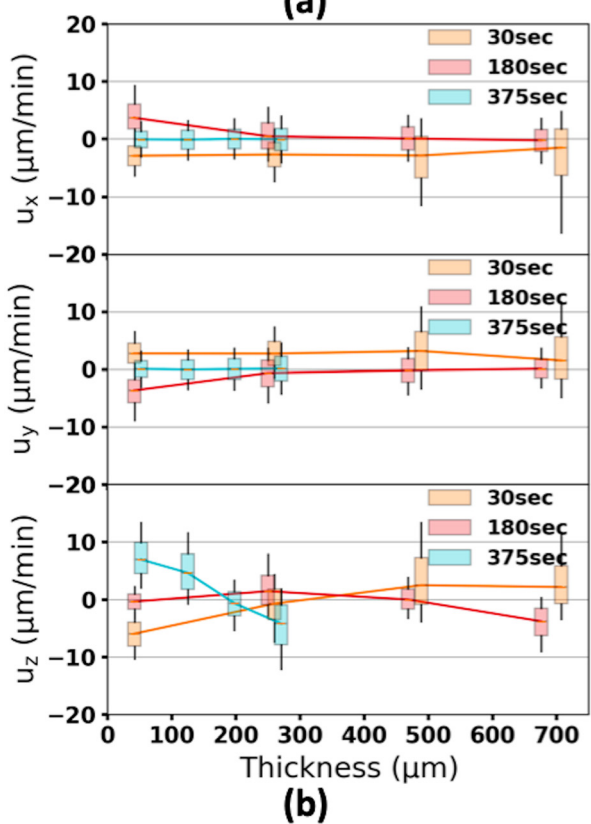


FIG. 2. Film drying local velocity z-component v_z map. (a) 3D distribution, and (b) three v components' median values in four layers at three time points. The box at each point indicates 95% confidence interval around the median value estimation. The whisker at each point marks the (10%, 90%) range of velocity value distribution in each layer.

the freedom of particles' motions in the x-y plane became smaller. Nonetheless, v_z showed interesting behavior along with the drying process. At the early stage of the drying process (30 s), the particles in the majority of film volume flew upward along with the solvent evaporation from the film-air interface. At the same time, the solvent close to the container wall flowed downward along the wall toward the bottom of the container to compensate for the loss of the solvent from the top surface. Therefore, the particles close to the container wall moved downward with the solvent flow. This is because the droplet of the slurry was larger than the container size in the beginning. Along with the solvent evaporation, some solvent outside the container flew into the container along the container wall. Overall, the top half of the film slightly moved upward along with the evaporation. The particles' motions in the top half of the film at this stage were more volatile than the later stages. This is evidenced by the larger uncertainties of the median values in the top two layers shown in Fig. 2(b). It should be noticed that the film-air interface at this stage was barely out of the camera's field of view, and so we could not see the interface. However, it is clearly seen that the trend of v_z change along the depth direction is different from the later stages.

At the later stage (180 s), the majority of particles in the volume below the interface mainly moved downward, while those in the bottom region moved upward. This is because, along with the solvent evaporation, the film-air interface moved down toward the container bottom; meanwhile, the solvent close to the container bottom flew upward to compensate the solvent loss from the surface. The downward flow along the container wall disappeared at this stage because the slurry droplet outside of the container dried out. The v_z distributions in each layer at this stage are smaller compared to the earlier and later stages, which are evidenced by the smaller v_z uncertainties in each layer. This is probably because the flow along the container wall disappeared, and the capillary effects among the particles were not significant yet. Specifically, the v_z distribution in the second layer had zero median value and smaller uncertainty compared to the first and third layers. This indicates that there was a less mobile zone between the upward solvent flow and the downward moving film-air interface.

At the late stage (375 s), the particles were more closely packed in the reduced volume after most solvent evaporated. The top half film volume shrank downward, while the solvent in the bottom half flew upward to compensate for the loss of the solvent. The motion of the particles close to the film-air interface was more turbulent at this stage than that at 180 s. The particles moved collectively in the top and bottom film regions, and there was a sharp boundary between these two regions. Similar to the 180-s stage, the ν_z distribution in the second layer had zero median value and smaller uncertainty compared to the first and third layers. It is also interesting to see that the top layers in both 180-s and 375-s stages had similar ν_z median values. This is not surprising since the film-air interface ν_z is linearly related to the solvent evaporation rate from the surface, which was a constant in the experiment at all stages.

The lower mobility of the layer just below the film-air interface may be directly related to the particles' packing in the final film. To reduce the pores and to have particles more closely packed, it is critical to have a sufficient time and room for the particles to move and land onto the drying front of the film. A too fast evaporation rate may trap particles and leave unfilled pores. Therefore, it is necessary to balance the solvent evaporation rate and the particle mobility in the region close to the film drying front. The film heating condition and the droplet compositions are critical factors in the drying process.

Differential tomography quantitative analysis provides the flexibility to have variable time gaps in the analysis. This is critical in studying a dynamic system like a drying film that has highly inhomogeneous structure evolutions. In the above analysis, the motion map at each time point combined the results with two different time gaps from the given time point. For instance, the v_z distributions in Fig. 2 were calculated with reconstructed tomography datasets during threetime windows. In the 375-second case, the three windows were $345-375 \text{ s} (t_1)$, $354-384 \text{ s} (t_2)$, and $360-390 \text{ s} (t_3)$, respectively. In some regions, the particles moved very fast, and so these regions reconstructed with the t_3 dataset look very different from that reconstructed with the t_1 dataset. Tomowarp2 failed in tracking motions in these regions. Instead, the structures reconstructed with t_2 and t_3 datasets were used in calculating the motions in these regions. The final result was then merged together with suitable scaling factors that compensate for the time gap difference.

Although, in principle, a motion map can be calculated from one pair of structures with a shorter time gap, the practical accuracy of the DVC method limits the smallest time gap that should be used in the calculation. The DVC analysis accuracy is data quality dependent. It is reasonable to use the mean values of the DVC result in an empty space to estimate the DVC analysis accuracy. In the film drying case, we determined $1.0~\mu\text{m/min}$ as the DVC analysis accuracy threshold according to the background analysis.

DVC relies on feature patterns to track motions. Compared to the conventional FXT data analysis approaches, which provide "static" 3D structure's snapshots of a dynamic system at different time points, the proposed approach provides the first-order differential maps of a dynamic system with respect to the time. The minimum subvolume in which there are well-recognized feature patterns sufficient enough for the comparison between two 3D structures determines the spatial resolution of DVC results. However, a too small subvolume would reduce the precision of DVC results. In general, the precision and spatial resolution of DVC results depend on the input data quality, the specific DVC algorithm in use, and the algorithm parameters. ^{23,24,31} Similarly, the achievable temporal resolution of the proposed method depends on if the structure of the sample system has a large enough change for the DVC algorithm to track. The difference has to be larger than the uncertainty associated with the DVC algorithm in use. In general, this limit depends on the sample systems themselves, the data quality, the DVC algorithm, and ultimately the single projection image acquisition

We present an analysis approach to quantitatively extract the dynamic information regarding the 3D microstructural evolution from continuous tomography measurements. We highlight here the utilization of the artifacts in the tomography reconstructions as fingerprints of structure features to track local structure changes. This strategy enables the detection of fast dynamic processes, which is beyond the detection limit of the conventional FXT method. This is conceptually similar to the optical speckle imaging approach widely used in strain measurements in mechanical tests, except that the "speckles" in this approach are sample's internal structure features together with the motion artifacts in tomographic reconstructions. Using this method, we measured the active particles' motions during the drying of the composite battery electrode. The result suggests that the particle

packing in the film depends on the balance between the solvent evaporation rate and the particle's mobility in the final drying stage. The direct observation of the drying process would help to build experiment-inspired multi-physics models that will deepen our understanding of these complex phenomena. This method is also applicable to a broad range of dynamic process studies, in which quantitative transient microstructural change information is desired.

See the supplementary material for additional details on the differential tomography data chunking scheme, a heuristic argument on the validity of differential tomography quantitative data analysis, numerical simulation, experimental data analysis, and sample preparation.

AUTHOR'S CONTRIBUTION

Y.Y. and Z.X. contributed equally to this work.

This research used resources of the Advanced Photon Source, a U.S. Department of Energy (DOE) Office of Science User Facility operated for the DOE Office of Science by the Argonne National Laboratory under Contract No. DE-AC02-06CH11357. This research used resources at the 18-ID FXI beamline of the National Synchrotron Light Source II, a U.S. Department of Energy (DOE) Office of Science User Facility operated for the DOE Office of Science by the Brookhaven National Laboratory under Contract No. DE-SC0012704. The Stanford Synchrotron Radiation Lightsource (SSRL) was supported by the U.S. Department of Energy (DOE), Office of Science, Office of Basic Energy Sciences under Contract No. DE-AC02-76SF00515. Yang Yang wants to acknowledge the European Synchrotron Radiation Facility (ESRF) for the computing resource to do data and image processing. The work at Virginia Tech was supported by the 4-VA Collaborative Research and National Science Foundation (No. CBET-1912885). The authors also thank the helpful discussions with Dr. Wah-Keat Lee and Dr. Yong Chu.

REFERENCES

- ¹C. Kumar, M. A. Karim, and M. U. H. Joardder, J. Food Eng. 121, 48 (2014).
- ²A. Mallik, MOJ Food Process. Technol. **6**, 400 (2018).
- ³E. K. Sahni and B. Chaudhuri, Int. J. Pharm. 434, 334 (2012).
- ⁴S. T. F. C. Mortier, T. De Beer, K. V. Gernaey, J. Vercruysse, M. Fonteyne, J. P. Remon, C. Vervaet, and I. Nopens, Eur. J. Pharm. Biopharm. **80**, 682 (2012).
- ⁵M. Schulz and J. L. Keddie, Soft Matter **14**, 6181 (2018).
- ⁶A. F. Routh, Rep. Prog. Phys. **76**, 046603 (2013).
- ⁷S. Jiang, A. Van Dyk, A. Maurice, J. Bohling, D. Fasano, and S. Brownell, Chem. Soc. Rev. 46, 3792 (2017).

- ⁸Y. Yang, R. Xu, K. Zhang, S. Lee, L. Mu, P. Liu, C. K. Waters, S. Spence, Z. Xu, C. Wei, D. J. Kautz, Q. Yuan, Y. Dong, Y. Yu, X. Xiao, H. Lee, P. Pianetta, P. Cloetens, J. Lee, K. Zhao, F. Lin, and Y. Liu, Adv. Energy Mater. 9, 1900674 (2019).
- ⁹C. Wei, S. Xia, H. Huang, Y. Mao, P. Pianetta, and Y. Liu, Acc. Chem. Res. 51, 2484 (2018).
- ¹⁰C. Tian, Y. Xu, D. Nordlund, F. Lin, J. Liu, Z. Sun, Y. Liu, and M. Doeff, Joule 2, 464 (2018).
- ¹¹L. Mu, Q. Yuan, C. Tian, C. Wei, K. Zhang, J. Liu, P. Pianetta, M. M. Doeff, Y. Liu, and F. Lin, Nat. Commun. 9, 2810 (2018).
- ¹²A. J. Shahani, X. Xiao, and P. W. Voorhees, Nat. Commun. 7, 12953 (2016).
- ¹³V. Vanpeene, J. Villanova, A. King, B. Lestriez, E. Maire, and L. Roué, Adv. Energy Mater. 9, 1803947 (2019).
- ¹⁴P. H. Kamm, F. García-Moreno, T. R. Neu, K. Heim, R. Mokso, and J. Banhart, Adv. Eng. Mater. 19, 1600550 (2017).
- ¹⁵E. Maire, C. L. Bourlot, J. Adrien, A. Mortensen, and R. Mokso, Int. J. Fract. 200, 3 (2016).
- ¹⁶S. J. Normile, D. C. Sabarirajan, O. Calzada, V. De Andrade, X. Xiao, P. Mandal, D. Y. Parkinson, A. Serov, P. Atanassov, and I. V. Zenyuk, Mater. Today Energy 9, 187 (2018).
- ¹⁷A. Nommeots-Nomm, C. Ligorio, A. J. Bodey, B. Cai, J. R. Jones, P. D. Lee, and G. Poologasundarampillai, Mater. Today Adv. 2, 100011 (2019).
- ¹⁸M. Ge, D. S. Coburn, E. Nazaretski, W. Xu, K. Gofron, H. Xu, Z. Yin, and W. K. Lee, Appl. Phys. Lett. **113**, 083109 (2018).
- ¹⁹K. Aditya Mohan, S. V. Venkatakrishnan, J. W. Gibbs, E. B. Gulsoy, X. Xiao, M. De Graef, P. W. Voorhees, and C. A. Bouman, IEEE Trans. Comput. Imaging 1, 96 (2015).
- ²⁰M. Odstrcil, M. Holler, J. Raabe, A. Sepe, X. Sheng, S. Vignolini, C. G. Schroer, and M. Guizar-Sicairos, Nat. Commun. 10, 2600 (2019).
- ²¹F. García-Moreno, P. H. Kamm, T. R. Neu, F. Bülk, R. Mokso, C. M. Schlepütz, M. Stampanoni, and J. Banhart, Nat. Commun. 10, 3762 (2019).
- ²²T. D. Schryver, M. Dierick, M. Heyndrickx, J. Van Stappen, M. A. Boone, L. Van Hoorebeke, and M. N. Boone, Sci. Rep. 8, 7655 (2018).
- ²³B. C. Roberts, E. Perilli, and K. J. Reynolds, J. Biomech. 47, 923 (2014).
- ²⁴A. Buljac, C. Jailin, A. Mendoza, J. Neggers, T. Taillandier-Thomas, A. Bouterf, B. Smaniotto, F. Hild, and S. Roux, Exp. Mech. 58, 661 (2018).
- 25B. A. Dowd, G. H. Campbell, R. B. Marr, V. V. Nagarkar, S. V. Tipnis, L. Axe, and D. P. Siddons, in *Developments in X-Ray Tomography II: Proceedings of SPIE 3772, Denver, USA, 18–23 July 1999*, edited by U. Bonse (SPIE, Bellingham, 1999), pp. 224–236.
- ²⁶M. L. Rivers, in *Developments in X-Ray Tomography VIII: Proceedings of SPIE 8506, San Diego, USA, 12–16 August 2012*, edited by S. R. Stock (SPIE, Bellingham, 2012), p. 85060U.
- ²⁷D. Gürsoy, F. De Carlo, X. Xiao, and C. Jacobsen, J. Synchrotron Radiat. 21, 1188 (2014).
- ²⁸E. Tudisco, E. Andò, R. Cailletaud, and S. A. Hall, SoftwareX **6**, 267 (2017).
- ²⁹I. Arganda-Carreras, V. Kaynig, C. Rueden, K. W. Eliceiri, J. Schindelin, A. Cardona, and H. S. Seung, <u>Bioinformatics</u> 33, 2424 (2017).
- 30 J. Schindelin, I. Arganda-Carreras, E. Frise, V. Kaynig, M. Longair, T. Pietzsch, S. Preibisch, C. Rueden, S. Saalfeld, B. Schmid, J.-Y. Tinevez, D. J. White, V. Hartenstein, K. Eliceiri, P. Tomancak, and A. Cardona, Nat. Methods 9, 676 (2012)
- ³¹E. Dall'Ara, M. Peña-Fernández, M. Palanca, M. Giorgi, L. Cristofolini, and G. Tozzi, Front. Mater. 4, 31 (2017).